Multiday Circulation and Precipitation Climatology during Winter Rain Events of Differing Intensities in Central Chile

BRADFORD S. BARRETT

Department of Oceanography, U.S. Naval Academy, Annapolis, Maryland

DOMINIQUE BASTINE KRIEGER

USS Rodney M. Davis, U.S. Navy

CAROLINE P. BARLOW

Department of Oceanography, U.S. Naval Academy, Annapolis, Maryland

(Manuscript received 13 September 2010, in final form 3 February 2011)

ABSTRACT

The majority of precipitation in central Chile falls during austral winter with the passage of surface and upper-level low pressure systems and their associated surface fronts. Earlier studies have found the presence of a terrain-parallel, low-level barrier jet during cold front passage and low-level wind convergence in the region of heaviest precipitation. This study advances these findings by developing multiyear climatologies for a rainfall event in central Chile using a broad cross section of observational datasets: the Tropical Rainfall Measuring Mission (TRMM), the Atmospheric Infrared Sounder (AIRS), the National Climatic Data Center (NCDC) Global Surface Summary of the Day (GSOD), the Integrated Global Radiosonde Archive (IGRA), the Quick Scatterometer (QuikSCAT), and the NCEP–NCAR reanalysis. For this study, a precipitation event was defined as daily rainfall exceeding a certain threshold at a Santiago observing station (Pudahuel). Climatologies were developed for a five-day period surrounding the precipitation event: the three days leading up to the day of precipitation at Pudahuel, the day of the precipitation itself, and the day after. Precipitation was found to move northeastward over the southeast Pacific toward central Chile and increase in intensity upon reaching reached the coast between 33° and 40°S. At middle levels, a pronounced 500-hPa trough moved eastward and amplified during the same period, and at the surface, an area of low pressure deepened and followed the same path to the east. In the boundary layer and lower troposphere, winds at 925 and 850 hPa became exclusively north-northwesterly, suggesting the existence of a low-level jet, and surface winds backed with time and increased in speed ahead of a well-defined cold front wind shift. As these winds became more northwesterly ahead of the upper-level trough and surface low, precipitable water values increased, and a tongue of high precipitable water air intersected the coast at the same location as the region of heaviest precipitation. These climatologies, based on hundreds of cases, together provide strong confirmation that forcing associated with an eastward-progressing upper-level trough, a terrain-parallel low-level wind maximum, and an advancing surface cold front together constitute the complex, complementary mechanisms for precipitation in central Chile.

1. Introduction

The densely populated central Chilean region, defined in this study to extend from 30° to 40°S along the west coast of South America, contains the majority of Chile's people (>8 million inhabitants), economic activities (agriculture, hydroelectric power, mining, and forestry), and government and military services (the capital, Santiago, and major ports of Valparaiso and Concepción). The region's topography varies considerably but is generally characterized by a coastal range, which rises to 700–1300 m immediately east of the coast, a central valley with a mean elevation of 500 m, and a sharp rise about 200 km inland to the summits of the Andes Cordillera. The Andes Cordillera is itself not uniform but rather varies in elevation

Corresponding author address: Bradford S. Barrett, Department of Oceanography, U.S. Naval Academy, 572C Holloway Rd., Annapolis, MD 21402.
E-mail: bbarrett@usna.edu

DOI: 10.1175/2011JHM1377.1

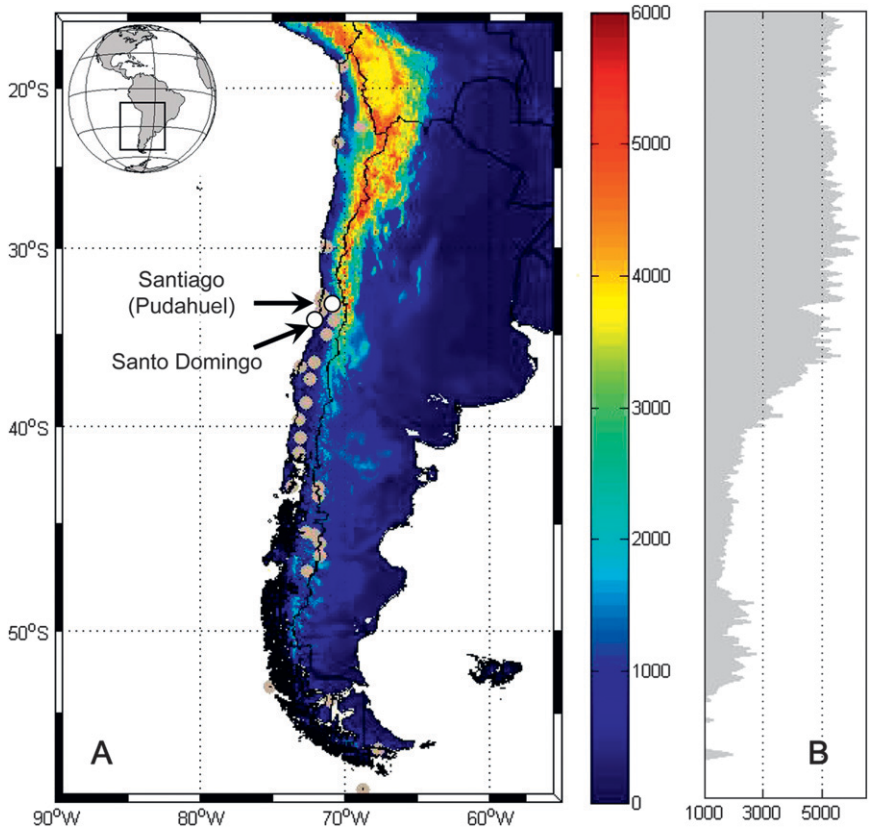

FIG. 1. (a) NCDC GSOD station locations (circles) and elevation (shading, m) of the southern Andean region and (b) maximum cordillera height (m) by latitude.

from over 6000 m in the north to less than 1500 m in the south (Fig. 1).

The central Chilean region exhibits a marine west coast climate, with the majority of precipitation falling in the winter season (Miller 1976). Just to its west lies one of the major global regions for surface and upper-level cyclogenesis (Hoskins and Hodges 2005). Low pressure systems that form in this area of the southeast Pacific move eastward, and as these low pressure systems and their associated cold fronts approach the western coast of South America during May–September, the cyclonic circulation and warm conveyer belt advect moist air from the subtropics poleward ahead of the cold front. This moist air rises as it approaches the coast in response to a combination of factors, including low-level wind convergence along the frontal surface (Barrett et al. 2009), upper-level height falls ahead of the midlevel trough, and orographic uplift (Falvey and Garreaud 2007). The resulting long-term mean precipitation in central Chile exhibits a strong meridional gradient with less than 100 mm per annum in the north (25°S) increasing to over 1500 mm per annum in the south (40°S), suggesting that the topography, which exhibits a gradient of the opposite sign, plays some role in determining precipitation climatology. Precipitation totals also exhibit a strong east–west gradient. Precipitation increases as one moves east from the southeast Pacific, reaching a maximum over the western slope of the Andes, and then decreases sharply again east of the continental divide with less than 400 mm year^{-1} in the semiarid climate of western Argentina.

As one of its mechanisms to affect precipitation, topography has been shown to modify airflow in many global regions, including the Cascades (e.g., Mass and Ferber 1990), the Sierra Nevadas (e.g., Marwitz 1987), Southern California (e.g., Hughes et al. 2009), the Alps (e.g., Kurz 1990; Bousquet and Smull 2006), the Appalachians (O'Handley and Bosart 1996), the Wasatch (Cox et al. 2005), and western Canada (Doyle and Bond 2001). One of the most prominent effects of mountains on the lower atmosphere is "upstream blocking" (Yu and Smull 2000) that arises as geostrophic balance breaks down in vicinity of the terrain. For the case of a steep, nearly two-dimensional barrier such as the central Andes, theory predicts that a major result of upstream blocking is the development of strong low-level flow parallel to the terrain axis (Parish 1982) resulting from downgradient

ageostrophic acceleration in the along-barrier direction (Overland 1984; Lackmann and Overland 1989). Low-level blocking is common in a small Froude number regime (U/Nh, where U is the speed of the free airstream, N is the buoyancy frequency, and h the terrain height; Doyle 1997). These ''barrier jet'' wind maxima then in turn interact with an approaching frontal system, causing it to deform and decelerate as it approaches the high terrain (Smith 1979). Viale and Norte (2009) examined a strong orographic precipitation event in the subtropical central Andes and found that a low-level along-barrier jet formed because of upwind flow blocking. Despite these observations, however, the disruption of weather systems, particularly cold fronts, along the upstream side of the south–central Andes has been less studied, in part because of the lack of data over the adjacent Pacific Ocean. Thus, one of the major goals of this study is to present a more comprehensive picture of the upstream atmosphere in the days preceding, during, and following a precipitation event in central Chile. Two recent studies have examined certain pieces of this atmosphere–topography interaction near the Andes—Barrett et al. (2009) (hereafter BGF09) and Falvey and Garreaud (2007) (hereafter FG07)—and here we briefly summarize their relevant findings as they relate to the climatologies of this study.

BGF09 examined the temporal and spatial evolution of precipitation, wind, and geopotential height during a cold front passage in May 2008 and found that three primary precipitation features were associated with the cold front: a ''Pacific precipitation zone'' (PPZ) located over the southeast Pacific west of the Chilean coast, a ''coastal precipitation zone'' (CPZ) extending from the eastern edge of the PPZ along the Chilean coast eastward to the Andes Cordillera, and a ''windward precipitation zone'' (WPZ) located over the high Andean terrain. One of their more interesting results was that both the cold front and the CPZ stalled over central Chile, leading to large rainfall amounts (greater than 60 mm) along the coast. Furthermore, the PPZ did not stall but continued to steadily progress northward, leading to deformation of the cold front. They also found a strong relationship between the location, structure, and evolution of the 925-hPa v-wind component and those of the precipitation. This setup is physically consistent with similar cold front–terrain interactions observed off the California coast (e.g., Doyle 1997; James and Houze 2005) and to observations from an event off Vancouver Island (Yu and Bond 2002), and suggests that the features observed in California, including a topographically forced barrier jet, may also be present in the central Andean region. These findings were noticed in both model and surface observations, leading BGF09 to hypothesize about their applicability to other cold front events. Thus, another of the goals of this study is to determine which, if any, of the features identified by BGF09 show up in a climatology comprised of hundreds of precipitation events (and both the low-level wind maximum and south-to-north precipitation gradient do appear in the climatologies presented later in this article).

Using rain gauges and stream flow data, FG07 also examined the impact of orography on precipitation structure in central Chile. They examined 228 winter-season rainy days from 1993 to 2002 and noted that, while the events frequently occurred on consecutive days, nearly all the events (98%) lasted no more than 3 days. From surface gauge, satellite, and reanalysis data, FG07 confirmed a well-defined north–south precipitation gradient during precipitation events, with heavy precipitation to the south and lighter amounts north. They also noted a characteristic cold frontal pattern in the precipitable water composites, with a ''long tongue of moist air impinging on central Chile'' with rainfall to its south. They examined the dependence of precipitation on selected variables from upper-air data at Santo Domingo (33°S) and found that most rain gauge stations had strong relationships between zonal moisture flux in the 2000–3000-m level. One of the (partially) unexplained findings from FG07 was the observed rainfall enhancement—including enhancement over the open ocean—west of the continental orography. FG07 speculated that this region of heavier rainfall was due to either rainy systems being ''triggered'' in situ or slowing of existing rainy systems as they moved east toward Chile. These unexplained findings provided additional motivation for our present study and prompted us to stratify our climatologies to examine synoptic differences during events of varying rainfall intensity.

Given the questions raised by BGF09 and FG07, the primary objective of this study is to describe the mean evolution of synoptic and mesoscale circulation and precipitation structure during rain events in central Chile using a broad array of datasets, and to particularly emphasize differences during rainfall events of varying intensities. To do this, we first develop climatologies from three remote sensing platforms: 1) precipitation using data from 10 years of observations by the Tropical Rainfall Measuring Mission (TRMM) satellite, 2) precipitable water content over the southeast Pacific from 7 years of Atmospheric Infrared Sounder (AIRS) satellite data, and 3) surface wind field using 7 years of Quick Scatterometer (QuikSCAT) data. Second, we develop a 33-yr climatology of lower-tropospheric flow (925–700 hPa) observed at the only regular radiosonde site in central Chile: Santo Domingo. We stratify the wind climatology by atmospheric stability (quantified by the

Froude number) and rainy days, noting the evolution of lower-tropospheric flow leading up to and during a rain event in central Chile. Third, we develop daily climatologies of 500-hPa geopotential height, mean sea level pressure, and u- and v-wind velocities for the 5-day period surrounding a rain event in central Chile from NCEP–NCAR reanalysis (Kalnay et al. 1996). Finally, we develop a precipitation climatology over Chile itself from 33 years of surface rain gauge data. The remainder of the paper presents our results and is organized as follows: in section 2 we discuss the datasets used in the analysis and define a ''precipitation event'' in central Chile; in section 3 we present the rainfall climatology derived from satellite, surface, and reanalysis data and a wind flow climatology from radiosonde data; and in section 4 we present several conclusions and a conceptual model for forcing of precipitation in the central Andean region.

2. Data and methodology

We used six key datasets, each with different record lengths, to produce the climatologies of this study: 1) TRMM, 2) AIRS, 3) the National Climatic Data Center (NCDC) Global Surface Summary of the Day (GSOD version 7), 4) the Integrated Global Radiosonde Archive (IGRA), 5) QuikSCAT, and 6) the National Centers for Environmental Prediction (NCEP)–National Center for Atmospheric Research (NCAR) reanalysis.

a. TRMM

We examined daily rainfall over the southeast Pacific and adjacent coastal Chile using observations from the TRMM satellite (Kummerow et al. 1998)—a joint project between NASA and the Japan Aerospace Exploration Agency (JAXA). Daily mean rain rate estimates in dataset 3B42, available from the Goddard Distributed Active Archive Center (GDAAC; http://daac.gsfc.nasa.gov/precipitation/data_access.shtml; described by Chiu et al. 2006), were examined for the period 2000–09—a total of 238 observations using the lowest rain threshold (observation counts are listed in Table 2; rain thresholds are described in section 3). This product is available on a $0.25° \times 0.25°$ latitude–longitude grid over the TRMM domain 50°N–50°S (Adler et al. 2000), and was generally available for the entire 10-yr period, with the exception of May 2009 and a few other days where the TRMM quality-control algorithm identified concerns. TRMM data has been used extensively in other global regions to create rainfall climatology and to examine spatial and temporal characteristics and variability (e.g., Rozante et al. 2010; Jiang and Zipser 2010) and also to study precipitation variability in a midlatitude frontal zone (e.g., BGF09; Han et al. 2009). We note that TRMM satellite precipitation estimates over complex topography are suspect, so for this study, we will focus on measurements west of the Andes Cordillera. Finally, to examine the relationship between open-ocean precipitation and sea level pressure, we superimposed 10 years of reanalysis sea level pressure onto the TRMM precipitation.

b. AIRS

In addition to precipitation, accurately measuring atmospheric water vapor is a challenging task given that moisture generally varies on smaller spatial scales in nature than do temperature or pressure (Raja et al. 2008). However, several recent studies have demonstrated that newly available space-borne hyperspectral infrared sounders, such as AIRS (Gautier et al. 2003), can be used to better understand variability of water vapor in the troposphere across various space and time scales (e.g., Gettelman and Fu 2008; Ryoo et al. 2008; Xavier et al. 2010). In this study, we use both the ascending and descending observations of total precipitable water from 2003 and 2005–09—a maximum of 148 observations for the least-restrictive rainfall threshold, taken at approximately 1330 and 0130 local time [see Gettelman et al. (2006) for a thorough review of precipitable water measurement by the AIRS instrument] to observe changes in precipitable water offshore of central Chile in the days leading up to a rainfall event in Santiago.

c. IGRA and GSOD

We also examined in situ surface and upper-air observations from Chile. The most relevant upper-air observations for the central Andes were taken at Santo Domingo (33.7°S and elevation 75 m; period of record 2002–present) and Quintero (32.8°S and elevation 5 m; period of record 1957–99). We are aware that the radiosonde launch moved in 1999 to its current location but believe that the dataset is reasonably homogeneous (FG07), and thus for this study we have chosen to treat both datasets as one continuous record, giving a maximum of 758 observations using the most-inclusive rain threshold. The NCDC IGRA (http://www.ncdc.noaa.gov/oa/climate/igra/index.php) maintains an archive of temperature, dewpoint temperature, geopotential height, and wind data for both of these stations. Surface precipitation data were obtained from 34 stations in Chile using the NCDC GSOD version 7 (available at http://www.ncdc.noaa.gov/cgi-bin/rs40.pl?page=gsod.html; see Table 1 and Fig. 1 for station names and locations). For this study, we defined a central Chilean ''rain event'' as one where daily rainfall exceeded a certain threshold at

TABLE 1. Station names, latitude, longitude, elevation (m above sea level), and period of record for the 34 GSOD locations (see Fig. 1 for location of each station).

Station name	Latitude	Longitude	Elevation (m)	Period of record
Arica	18.5°S	70.2°W	58	1977–2009
Iquique	20.5°S	70.2°W	47	1984–2009
Calama	22.5°S	68.9°W	2320	1977–2009
Antofagasta	23.4°S	70.5°W	140	1977–2009
La Serena	29.9°S	71.2°W	146	1977–2009
Quintero	32.8°S	71.5°W	5	1977–2009
Punta Angeles	33.0°S	71.6°W	41	1985–2009
Viña del Mar	33.1°S	71.6°W	342	1977–2009
Pudahuel	33.4°S	70.8°W	474	1977–2009
Quinta Normal	33.4°S	70.7°W	520	2006–2009
Santiago	33.5°S	70.6°W	649	1984–2009
Juan Fernández	33.6°S	78.8°W	30	1977–2009
Santo Domingo	33.7°S	71.6°W	75	1977–2009
De la Independencia	34.2°S	70.8°W	441	1977–2009
Curicó	35.0°S	71.2°W	225	1977–2009
Chillán	36.6°S	72.0°W	148	1977–2009
Concepción	36.8°S	73.1°W	148	1977–2009
Los Ángeles	37.5°S	72.4°W	114	2005–2009
Temuco	38.8°S	72.6°W	114	1977–2009
Valdivia	39.6°S	73.1°W	19	1977–2009
Osorno	40.6°S	73.1°W	65	1977–2009
Puerto Montt	41.4°S	73.1°W	90	1977–2009
Quellón	43.1°S	73.6°W	4	1977–2009
Futaleufú	43.2°S	71.8°W	350	1977–2009
Alto Palena	43.6°S	71.8°W	277	1977–2009
Puerto Aisén	45.4°S	72.7°W	11	1977–2009
Coyhaique	45.6°S	72.0°W	343	1977–2009
Balmaceda	45.9°S	71.7°W	525	1977–2009
Chile Chico	46.6°S	71.7°W	326	1977–2009
Cochrane	47.2°S	72.6°W	182	1977–2009
Faro Evangelistas	52.4°S	75.1°W	52	1977–2009
Punta Arenas	53.0°S	71.0°W	37	1977–2009
Puerto Williams	54.9°S	67.6°W	23	1977–2009
Isla Diego Ramírez	56.5°S	68.7°W	42	1977–2009

Pudahuel (33.4°S, elevation 474 m, and location of the international airport). The precipitation data were transformed from an ungridded into a gridded dataset using the thin-plate smoothing spline function native to Matlab. Commonly used thresholds were 1) at least 0.25 mm (0.01 in., which is the smallest increment of rainfall available in the GSOD dataset), 2) at least 12.5 mm (0.50 in.), and 3) at least 25.4 mm (1.00 in.; see Table 2 for record lengths). The heavy rainfall threshold 2 represents the upper 4.6% of all rainfall events. We selected the observing station at Pudahuel for two reasons: first, it has a long uninterrupted period of record (1973–2009), and second, it is representative of rainfall over the densely populated central valley.

d. QuikSCAT and reanalysis

The fourth dataset, QuikSCAT (Ebuchi et al. 2002), uses microwave sensors to retrieve the surface wind speed and direction over the open ocean. The level 3 data are available at approximately 0.5° × 0.5° latitude–longitude grid, and we examined 7 years of data from 2003 to 2009 (a maximum of 148 observations). Finally, to complement the remote sensing and in situ datasets discussed above, we analyzed upper-air data from the NCEP–NCAR reanalysis (Kalnay et al. 1996), available daily on a 2.5° × 2.5° latitude–longitude grid.

3. Daily climatologies

Each of the climatologies presented in this section were developed using the following method: first, a rain event at Pudahuel was selected using a specific 24-h precipitation threshold (e.g., >0.25 mm in a day, >25.4 mm in a day, etc.; see Table 2 for the period of record and number of observations available for each threshold). Lighter precipitation threshold subsets include the heavier-event subsets. Second, data from the various datasets (TRMM, AIRS, NCEP–NCAR reanalysis, QuikSCAT, IGRA, and GSOD) were aggregated for each day that met the rainfall threshold, as well as the three days before and the day after, for a total of five days for each event. Finally, the aggregate data were averaged to produce daily means. Day 4, the day with rain in central Chile at Pudahuel, will be referred to as the precipitation event (PE). We recognize that PEs in central Chile often occur over multiple days. However, when we filtered the precipitation datasets to select only the heaviest 24-h rainfall of a multiday PE, the climatologies did not materially change (not shown). Therefore, each 24-h period with measurable precipitation was considered as its own PE when developing the climatologies.

Ten years of TRMM satellite data—a total of 238 observations—were averaged to produce a climatology showing the progression of open-ocean precipitation

TABLE 2. Numbers of precipitation events (PEs) for each climatology dataset, stratified by rainfall threshold.

Relevant climatology Rain threshold (mm)	IGRA 1973–2009	GSOD and reanalysis 1977–2009	TRMM 2000–09	AIRS and QuikSCAT 2003–09
≥0.25	758	694	238	148
≥12.5	187	158	52	29
≥25.0	85	62	17	7

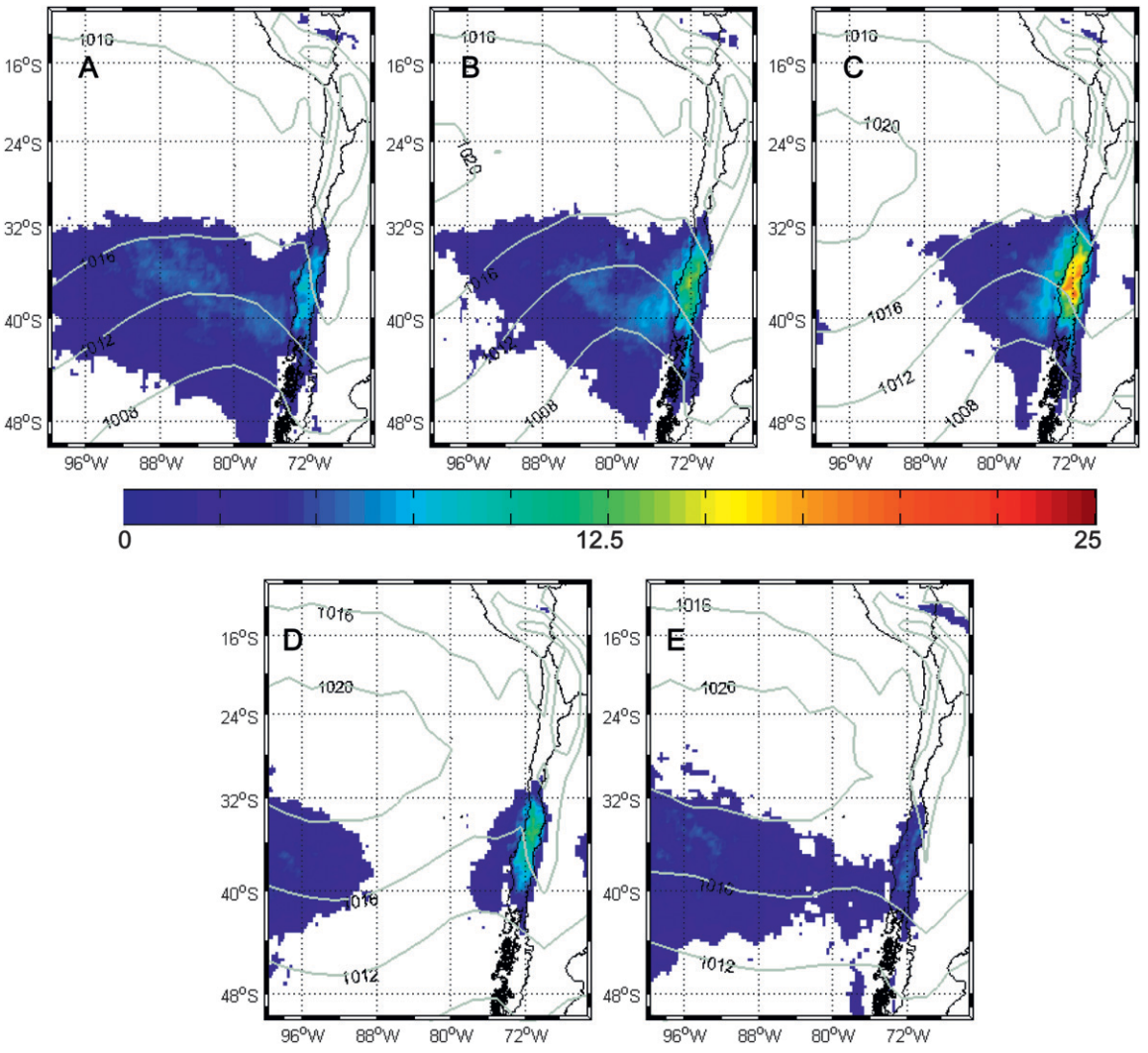

FIG. 2. Mean TRMM daily rainfall estimates (mm) and reanalysis sea level pressure (mb) for (a) 3 days before at least 0.25-mm rainfall at Pudahuel, (b) as in (a), but 2 days before rainfall at Pudahuel, (c) as in (a), but 1 day before, (d) as in (a), but for the day of rain at Pudahuel, and (e) as in (a), but for 1 day after rain at Pudahuel.

lead-up to, and following, a PE of at least 0.25 mm in the central Andean region. Figure 2 shows that three days before rain fell in Pudahuel, a large region of precipitation extended several thousand kilometers offshore of Chile into the southeast Pacific. This region is likely broader than what would be observed during an individual PE, owing to smoothing induced by averaging over 238 observations. Precipitation intensities increased from west to east, reaching a maximum just along the Chilean coast between 36° and 40°S (Fig. 2a). This broad precipitation region roughly corresponds with the PPZ identified by BGF09. As the low pressure system approached central Chile, it deepened, and the west-to-east gradient in precipitation intensity strengthened, particularly in precipitation intensities along the coast. This region of precipitation, both its location and characteristic increase in precipitation intensity, corresponds to another precipitation zone identified by BGF09: the CPZ (Fig. 2b). Once the surface low reached the coast (Figs. 2c,d), open-ocean precipitation rapidly diminished, while coastal precipitation remained stationary and oriented nearly parallel to the terrain. Finally, after the PE (Fig. 2e), the precipitation gradient reversed, and precipitation was greatest near 100°W as the next weather system developed. Interestingly, for central Chilean PEs, precipitation intensities were maximized between 32° and 40°S and diminished substantially in southern Chile and the southern Pacific south of 40°S.

In addition to mean precipitation from the TRMM satellite, seven years of AIRS precipitable water (PW)

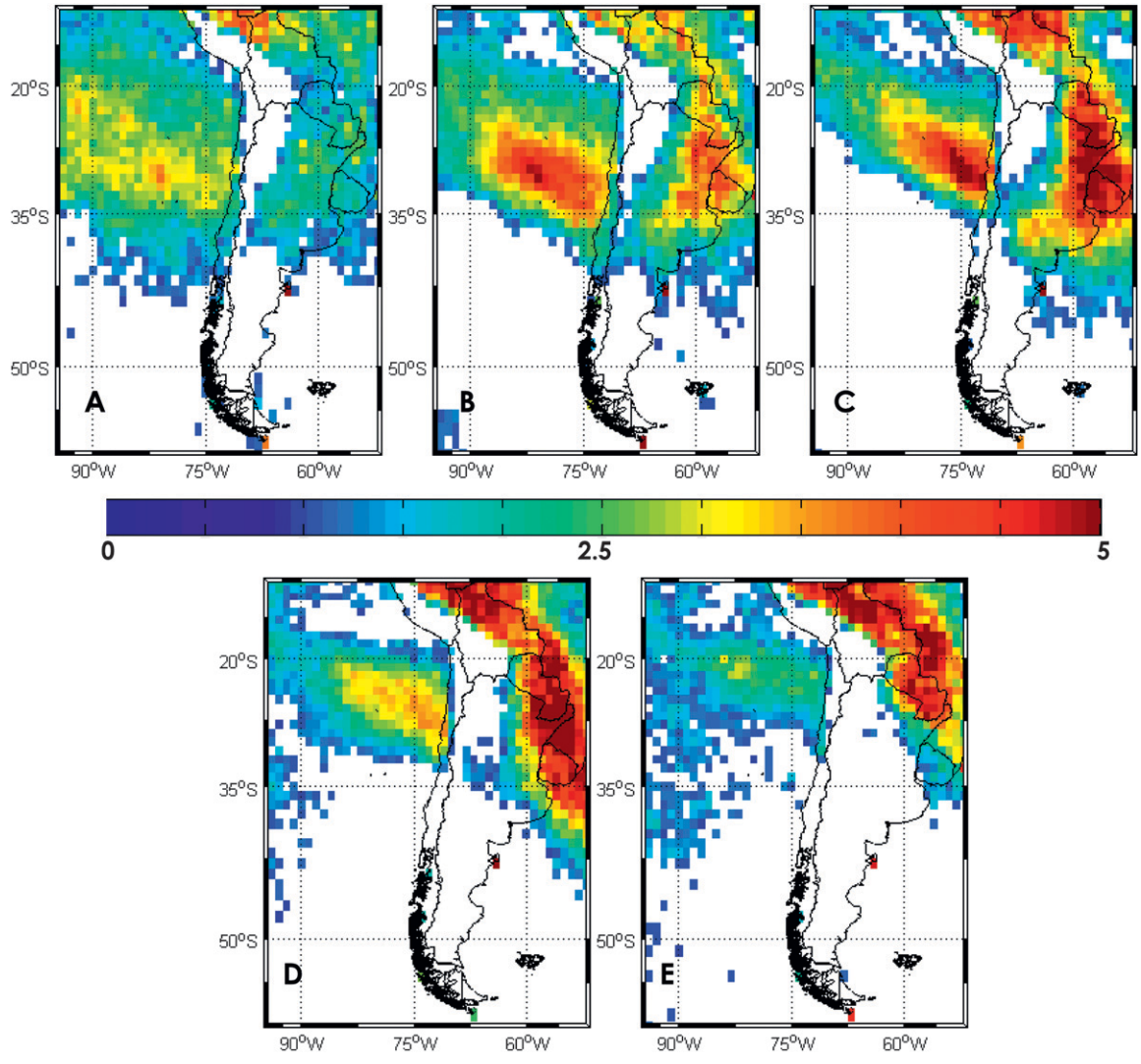

FIG. 3. As in Fig. 2, but for mean AIRS total precipitable water anomalies (mm).

data—a total of 148 observations—were averaged to examine the progression of PW in the three days leading up to, the day of, and the day following a PE in the central Andean region. The general PW climatology in austral winter is characterized by high PW over the Amazon basin of Brazil, Bolivia, Paraguay, and Peru, and by low PW content over the Atacama and high cordillera of northern Chile, northwest Argentina, southwest Bolivia, and southern Peru (Labraga et al. 2000). To highlight the departure from this synoptic mean during a PE, we show PW anomalies (Fig. 3). In the days leading up to a PE in central Chile, anomalously high PW was observed from the tropical regions south–southeast toward the coast, in an axis from 20°S, 90°W southeast to 35°S, 75°W. This anomalously high PW content—up to 5 mm higher than the May–August synoptic mean—extended from the tropical South Pacific into the subtropics between 20° and 35°S. This axis shifted slowly northward as the low approached the coast (Figs. 3a–c), likely in response to the equatorward progression of the surface cold front behind the low. It is important to note that this axis of higher PW content air intersected the coast in the same general location as the northern extent of heavy precipitation observed by the TRMM satellite (Figs. 2b,c). Furthermore, the axis of high PW content was oriented parallel to and intersected the coast around the location of the entrance region of the low-level northerly barrier jet (see following paragraph).

Surface wind data from QuikSCAT confirm the development of a strong north–northwesterly wind maximum just offshore in the days leading up to a PE in central Chile (Fig. 4). The general surface flow (Fig. 4a)

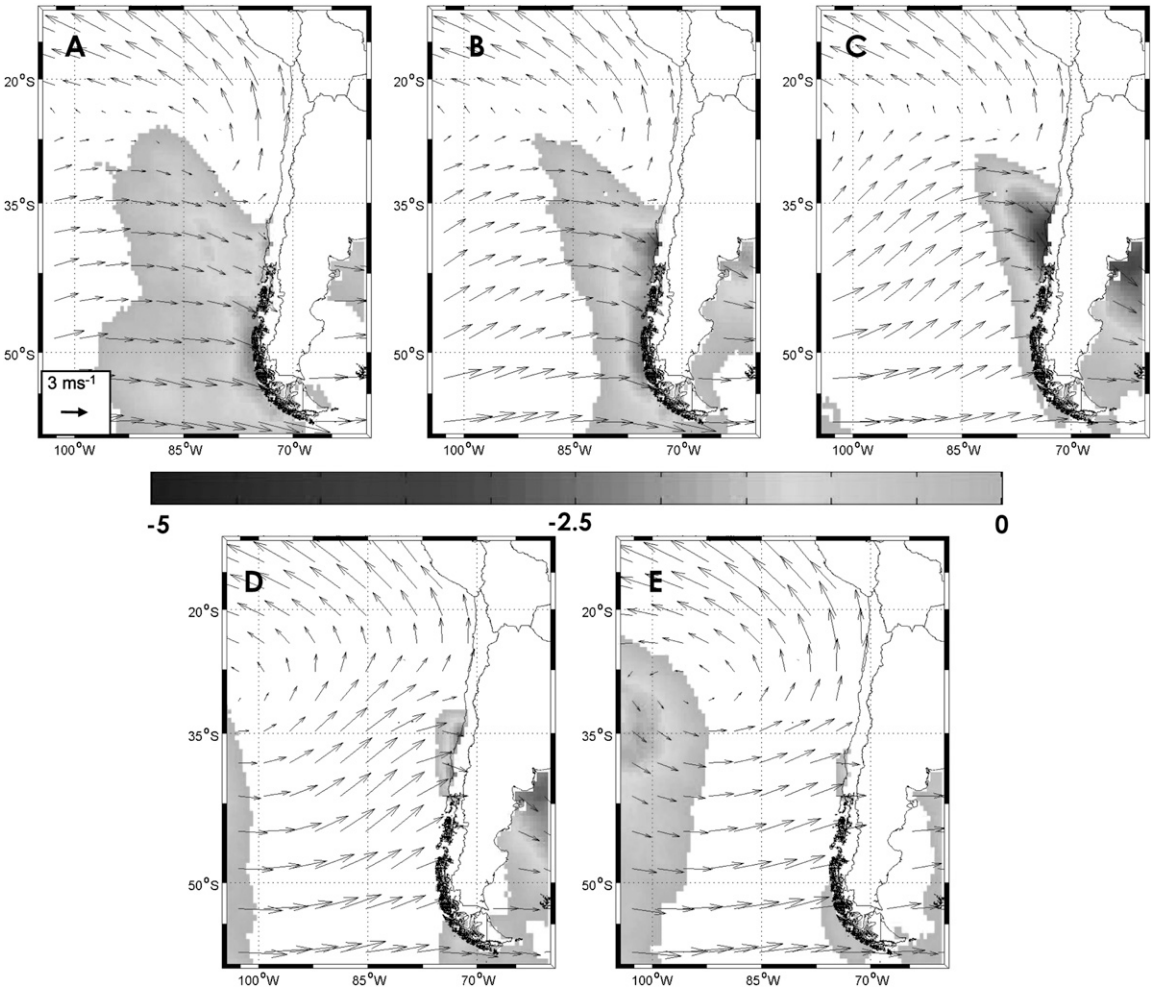

FIG. 4. As in Fig. 2, but for mean QuikSCAT surface wind vectors (arrows, m s^{-1}) northerly flow (gray scale, m s^{-1}).

is characterized by an anticyclone centered between 2000 and 3000 km west–northwest of central Chile, with broad anticyclonic flow surrounding the high center and an eastward-progressing wind shift, which would be associated with the synoptic-scale cold front, approaching the Chilean coast (Fig. 2). In the 24- to 48-h period prior to the PE, surface winds between 32° and 37°S became more northerly ahead of the approaching cold front and increased from less than 2 to over 5 m s^{-1}, forming a terrain-parallel low-level barrier jet (Figs. 4b,c). The placement and strength of this northerly jet is in agreement with earlier observations (e.g., BGF09 and Smith 1979), and the wind maximum intersected the Chilean coast between 36° and 38°S (Fig. 4c), at approximately the same location as the local precipitation maximum (Figs. 2b,c) and tongue of higher precipitable water (Fig. 3b), and just south of the IGRA upper-air station at Santo Domingo (following paragraph). Southwesterly surface winds behind the cold front reached the coast by the day of the PE (Fig. 4d) and also intersected the northerly barrier jet at the same location as the heaviest precipitation totals. By the day after the PE (Fig. 4e), the surface anticyclone had shifted 1000 km closer to the coast and surface southwesterly flow prevailed at the coast (Fig. 2e). For PEs greater than 12.5 mm, surface northwesterly (southerly) flow was up to 5 m s^{-1} (10 m s^{-1}) stronger ahead of the cold front (Fig. 5) when compared to all PEs (Fig. 4), especially the day of the PE (Fig. 5d).

IGRA upper-air data also show the development and progression of a low-level, terrain-parallel wind maximum jet (Fig. 6). Three days before a PE in central Chile, 925-hPa winds were distributed in a bimodal manner, with nearly equal northerly and southerly frequencies (Fig. 6a). As a low pressure system approached the coast in the 24–48-h period before a PE, 925-hPa winds became almost entirely northerly and velocities increased (Figs. 6b–d). After the precipitation-producing system passed,

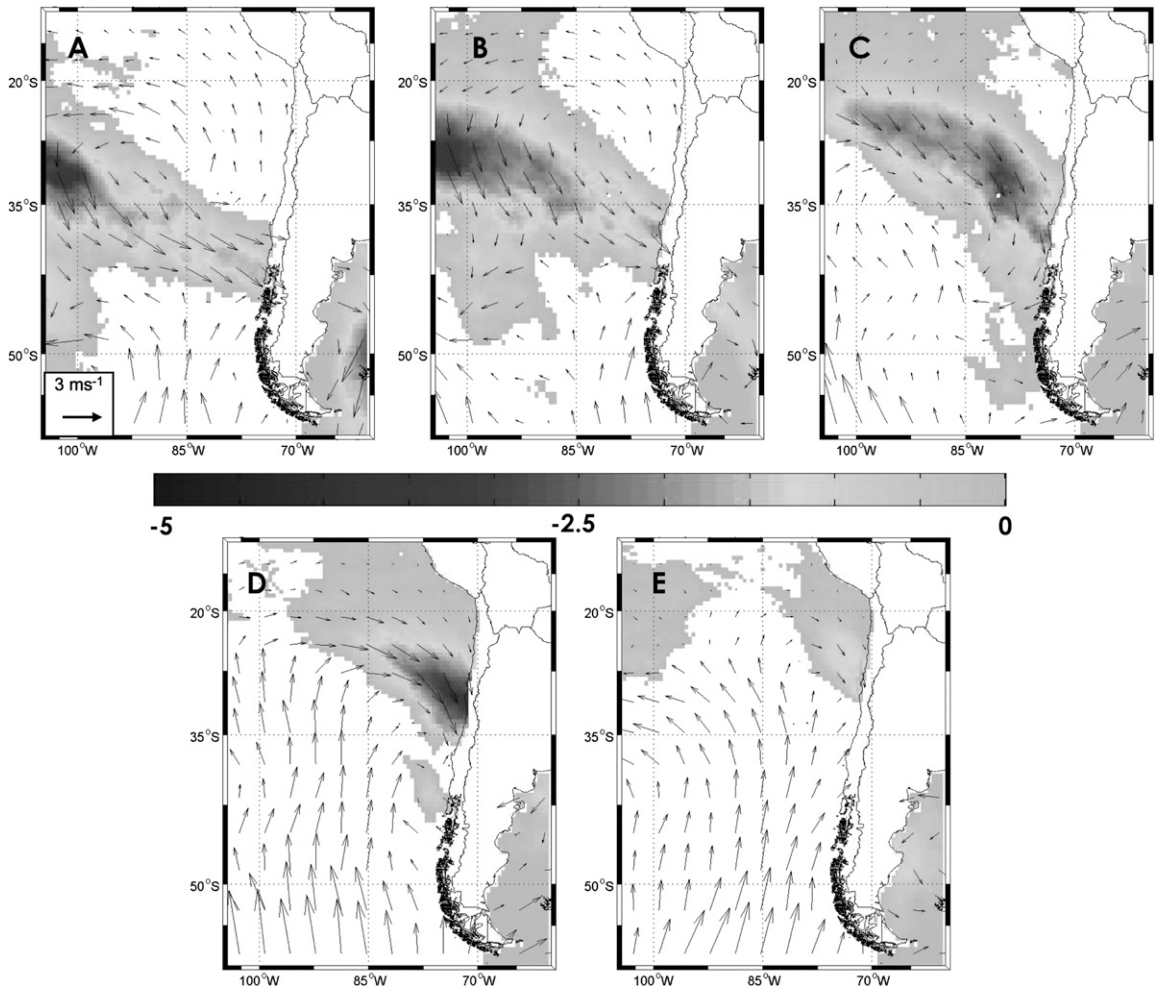

FIG. 5. As in Fig. 4, but for mean QuikSCAT surface wind anomalies for precipitation events >12.5 mm (anomalies calculated from wind field for precipitation events >0.25 mm).

925-hPa flow returned to a bimodal distribution with the return of south–southeasterly winds (Fig. 6e). Boundary layer changes leading up to a PE were less noticeable at 850 and 700 hPa, but the 850-hPa winds still exhibited an increase in terrain-parallel north–northeasterly winds in the days before the PE and then returned to southerly flow after a PE. Winds at 700 hPa exhibited veering from northwest to more west–northwest in response to the approach of the upper-level trough. To examine the effects of flow blocking, we stratified the sounding data by Froude number:

$$\mathrm{Fr} = \frac{U}{Nh}, \tag{1}$$

where U is the airstream speed orthogonal to the topographic barrier (which, for the Andes, is simply the east–west velocity component), N the Brunt–Väisälä frequency, and h the mountain height. We used 4000 m for the mean height of the Andes because it roughly corresponds to the elevation of the lowest pass east of the radiosonde location (Cristo Redentor) and because the mean cordillera height between 35° and 40°S is around 4000 m. Because relative humidity affects the buoyancy frequency and thus the amount of topographic blocking (Durran and Klemp 1982), we used two forms of the Brunt–Väisälä frequency, depending on the degree of saturation. When relative humidity was less than 90%, the dry Brunt–Väisälä frequency N_d was used:

$$N_d^2 = \frac{g}{\theta_v}\frac{d\theta_v}{dz}, \tag{2}$$

where g is the gravitational acceleration (9.81 m s^{-2}) and θ_v the virtual potential temperature. When relative humidity was greater than or equal to 90%, we used the moist Brunt–Väisälä frequency N_m:

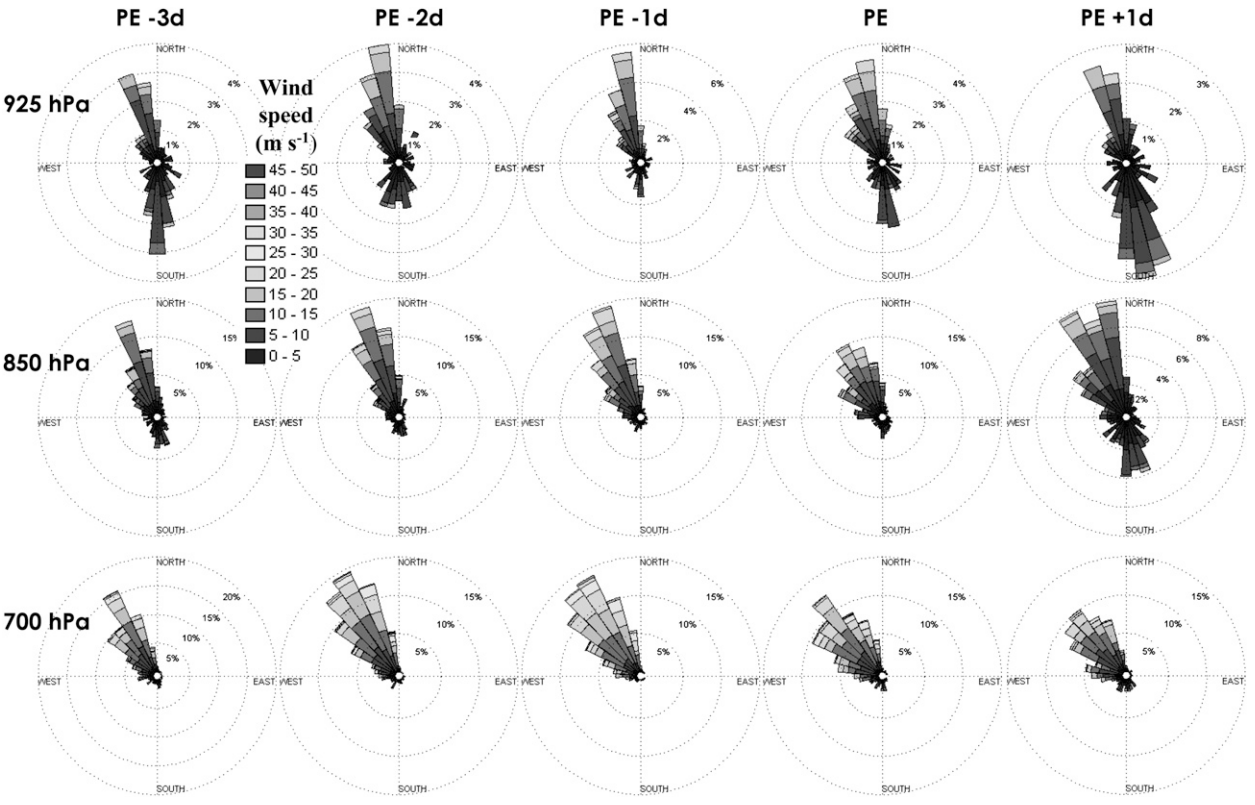

FIG. 6. (top to bottom) Mean 925-, 850-, and 700-hPa wind direction frequency (wind rose vector length) and speed (wind rose vector gray shade) at Santo Domingo for (left to right) 3 days prior to a PE, 2 days prior, 1 day prior, the day of the PE, and 1 day after.

$$N_m^2 = \left(\frac{g}{T}\frac{dT}{dz} + \Gamma_m\right)\left(1 + \frac{Lq}{R_d T}\right) - \frac{g}{1+q}\frac{dq}{dz}, \quad (3)$$

where T is air temperature (K), Γ_m the moist (pseudo) adiabatic lapse rate, L the latent heat of vaporization (2.5×10^6 J Kg^{-1}), q the water vapor mixing ratio (kg kg^{-1}), and R_d the dry gas constant (287 J kg^{-1} K^{-1}). We selected 90% as our threshold following Hughes et al. (2009), who found the frequency to be ''insensitive to moderate variations of the relative humidity threshold (i.e., between 85% and 95%).'' We calculated Froude numbers at the 925-, 850-, 700-, and 500-hPa levels (see Table 3). Froude numbers of 0.3 provided a natural break point in the lower-troposphere wind direction data, with the slow, very stable (Fr < 0.3) flow regimes characterized by nearly unidirectional southeast flow and the more unstable, faster regimes (Fr > 0.3) characterized by nearly unidirectional northwest flow. Not surprisingly, most of the Froude numbers in the lower troposphere (at and below 700 hPa) were low (<0.3), implying the flow was blocked (Smith 1979). Only at 500 hPa did Froude numbers approach 0.5 (see Table 3), indicating the flow was unblocked (Baines 1987). When Froude numbers were below 0.3, boundary layer flow had a significant southeasterly component (Fig. 7a). However, when the Froude number increased above 0.3 as a result of either faster flow more orthogonal to the barrier (larger U) or advection of moister, more unstable air (smaller N), boundary layer flow was almost exclusively north-northwesterly (Fig. 7b). Because PEs were also characterized by north-northwesterly boundary layer flow (Figs. 6b–d), this low-level wind maximum likely played a significant role in transporting moister, more unstable air into central Chile during a PE.

GSOD data were used in combination with 500-hPa geopotential height and wind to examine the development and progression of precipitation over land and

TABLE 3. Numbers of soundings at Santo Domingo from 1973 to 2009 with Froude numbers (Fr) below or above certain thresholds, stratified by pressure level.

Pressure level (hPa)	Fr < 0.3	Fr ≥ 0.3	Fr ≥ 0.5	Fr ≥ 1.0
925	7616	99	25	3
850	9788	160	24	2
700	9109	896	78	1
500	3053	8234	4644	228

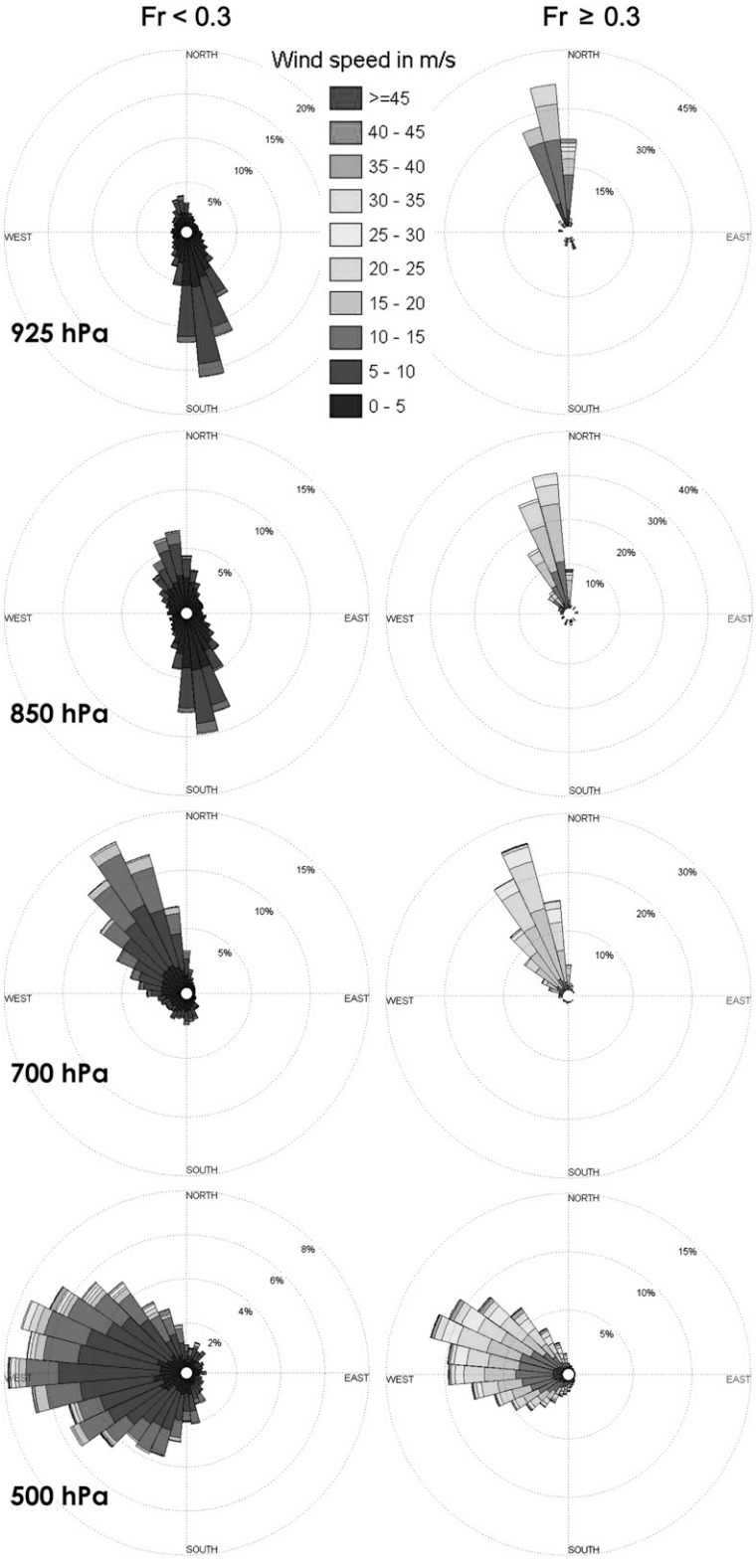

FIG. 7. (top to bottom) Mean 925-, 850-, 700-, and 500-hPa wind direction frequency (wind rose vector length) and speed (wind rose vector color) at Santo Domingo for PEs with Froude number (left) < 0.3 and (right) ≥ 0.3.

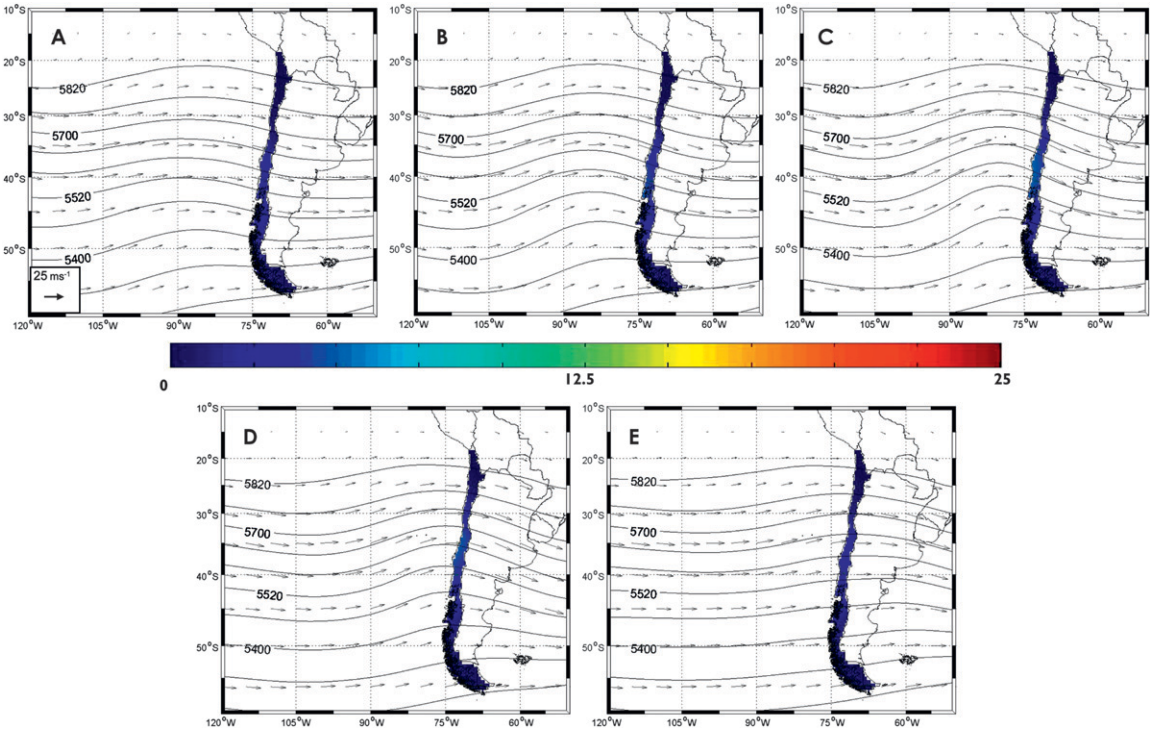

FIG. 8. As in Fig. 2, but for mean GSOD gauge precipitation (colors, mm), reanalysis 500-hPa geopotential height (contours, m), and 500-hPa wind (arrows, m s^{-1}).

its connection to forcing from the middle and upper troposphere. Three climatologies were created by varying the rainfall threshold to determine a PE: daily rainfall at Pudahuel greater than 0.25, 12.5, or 25.4 mm. For the most-inclusive rainfall threshold (greater than 0.25 mm, 694 cases in 33 years; Fig. 8), it is clear that three days before rain fell in central Chile, a 500-hPa trough was located 2000 km to the southwest and light precipitation (between 0 and 5 mm day^{-1}) was just beginning along the south–central Chilean coast (Fig. 8a). As this trough approached the coast and deepened, precipitation increased in intensity (to between 5 and 10 mm day^{-1}) and moved northward (Figs. 8b–d). Maximum precipitation intensity occurred 200–400 km south of the greater Santiago area, roughly between 36° and 38°S (Figs. 8c,d). By the day of the PE (Fig. 8d), the 500-hPa trough had nearly reached the coast and precipitation intensities in south–central Chile (near 40°S) had begun to decrease. By the day after the PE (Fig. 8e), the 500-hPa trough axis had reached the coastline, and precipitation intensities had decreased over all of central Chile. The presence of a mean trough at 500 hPa that moves east with the precipitation in a climatology comprising more than 700 cases in a 33-yr period provides strong confirmation that precipitation in central Chile is controlled by forcing provided by passing midlatitude waves. Additional evidence for this relationship was found by increasing the rain threshold used to define a PE. For PEs with at least 12.5 mm, the general upper-level pattern was similar to that of the lower precipitation threshold: a mean trough at 500 hPa that progressed eastward with time, reaching the coast the day after the PE (Fig. 9). However, the 500-hPa trough was more amplified, especially between 24 and 48 h prior to the PE, with geopotential height more than 40 m lower than mean heights for all PEs (Figs. 9b,c). As a result, precipitation intensity was greater and the precipitation began in central Chile about 12 h earlier. For the heavy PE (a threshold of >25.4 mm in one day, represented by 62 cases), the 500-hPa trough was even more amplified with geopotential height anomalies over 80 m (Fig. 10), and not as progressive, with the axis still over 1000 km west of the Chilean coast the day after the PE (Fig. 10e). Precipitation intensity was greatest when the 500-hPa trough was most amplified and located about 1500 km west of the coast (Fig. 10d) and when a precipitation intensity region >25 mm day^{-1} extended equatorward nearly to 30°S and >10 mm day^{-1} extended to nearly 25°S.

4. Conclusions

Using six different remote sensing and in situ observational datasets, we created five-day climatologies for

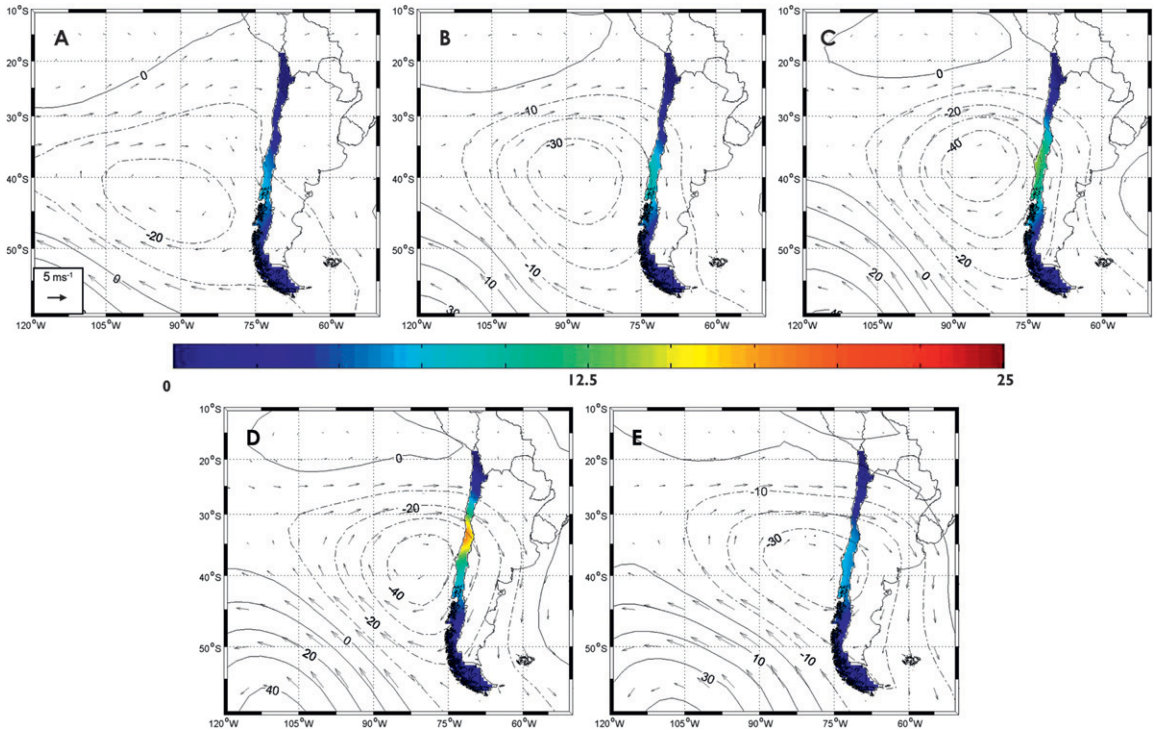

FIG. 9. As in Fig. 8, but with geopotential height (m) and wind (m s^{-1}) anomalies at 500 hPa associated with a PE rainfall threshold of 12.5 mm. Anomalies are calculated with respect to mean 500-hPa height and wind for all PEs.

winter-season rainfall events in central Chile. TRMM, GSOD, and surface pressure data revealed that 48–72 h before rain in Pudahuel, precipitation accompanying an area of surface low pressure moved east and east-northeast from the SE Pacific toward south central Chile. As this precipitation reached the coast, rainfall intensities (surface pressures) increased (decreased), reaching a maximum (minimum) along the coast a few hundred kilometers south of Santiago. Reanalysis data also revealed that a mean 500-hPa trough progressed eastward in tandem with the precipitation. When the mean midlevel trough was most amplified and slowest, rainfall totals during the PE were highest, longest lived, and extended farthest equatorward. We believe this pattern, supported by several hundred historical cases, provides strong evidence confirming that midlevel waves and their associated surface lows provide forcing for precipitation in central Chile, especially the heaviest PEs.

Additional evidence for precipitation forcing is found in QuikSCAT and IGRA data. Both climatologies revealed that a low-level, terrain-parallel wind maximum developed and intensified in the 24–48-h period prior to a PE, reaching maximum intensity about 24 h before a PE. Upper-air data showed that this wind maximum was concentrated near 925 hPa and most pronounced when the Froude number was largest, indicating lowest atmospheric stability and fastest midlevel flow. QuikSCAT data captured the surface reflection of this wind maximum, which developed about 24 h prior to a PE, extended 300 km northeast of the coast, and was most intense during the heaviest PEs. A larger surface wind shift located to the southwest of the barrier jet progressed eastward and equatorward in tandem with the precipitation region in association with the synoptic cold front. This surface wind shift intersected the coast at the same location as the maximum in the low-level wind maximum. AIRS data showed a tongue of high precipitable water air arcing southeast from the tropical Pacific, also intersecting the coast at the same time (24 h before a PE) and location (near 36°S) as the surface wind shift and the low-level jet maximum at a ''triple point'' between the cold front, low-level wind maximum, and the Andes. Not surprisingly, therefore, the heaviest precipitation region was collocated here in time and space.

We believe that these surface data complete the conceptual model, providing additional evidence of forcing for precipitation in central Chile. Our model, therefore, is as follows: a midlevel wave and associated surface low and cold front progress eastward toward central Chile, bringing a region of light–moderate precipitation over the open ocean. As this weather system approaches the coast, about 24 h before onset of precipitation in central Chile,

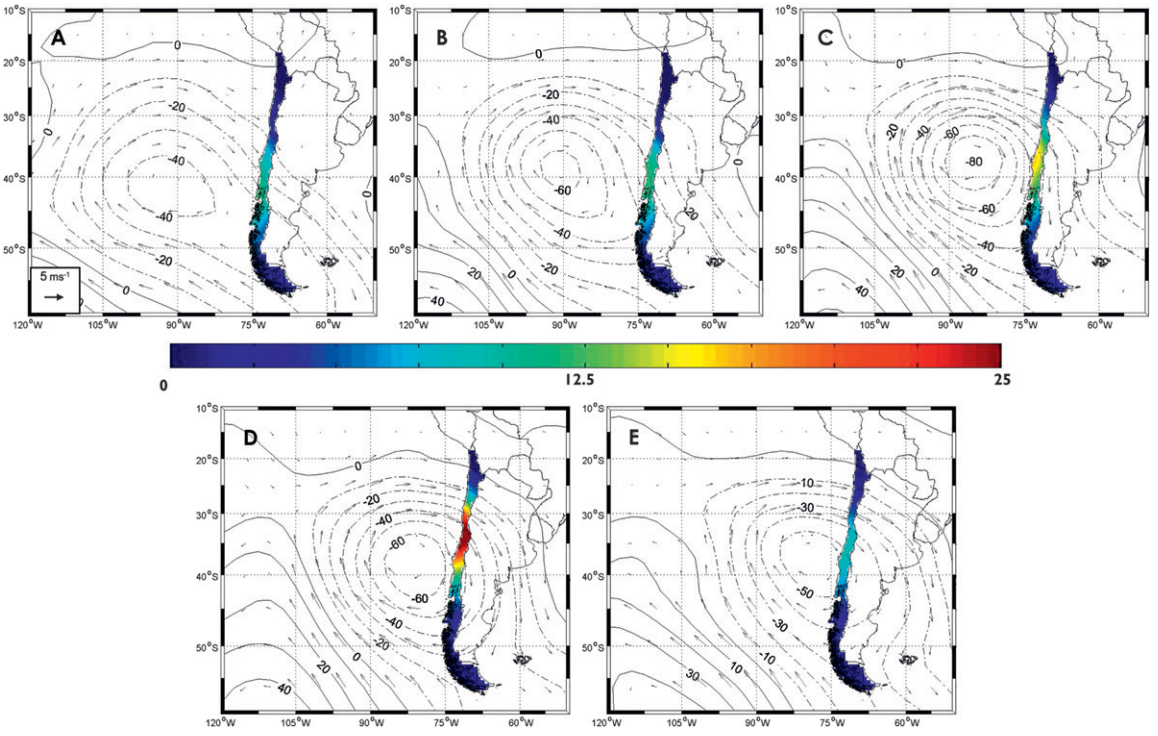

FIG. 10. As in Fig. 8, but for 500-hPa height and wind anomalies associated with a PE rainfall threshold of 25 mm.

a low-level wind maximum develops and intensifies as surface pressures fall with the approaching low. Given the results from BGF09 and our finding that Froude numbers for parcels below 850 hPa rarely rise above 0.5, we believe this wind maximum is a barrier jet that develops as a result of flow blocking by the Andes. However, we acknowledge the difficulty in separating the synoptic contribution to the wind maximum associated with the cold front from the mesoscale contribution associated with flow blocking by the Andes. This question remains unresolved and an area for future study. Regardless of its forcing, the wind maximum aligns with the tongue of high precipitable water anomalies, suggesting it aids in synoptic and mesoscale transport of moisture-rich air southward from the tropical Pacific. With the surface cold front to the west and the Andes Mountains on the east, this tongue of moist air is channeled toward central Chile. Rainfall intensities increase from north to south as the upper wave approaches and reach a maximum near 36°S at a triple point of the intersection of the moisture axis, low-level wind maximum, and cold front; possibly explaining the observed climatological precipitation maximum there. Rainfall ends, the low-level wind relaxes, and precipitable water content decreases once the upper trough axis passes to the east of the Andes. The more amplified and slower moving the upper-level trough is, the greater the total rainfall; a less amplified and quicker-moving trough produces less rainfall.

Acknowledgments. Funding for this work was provided by the Naval Academy Research Council via the Office of Naval Research. The authors thank René Garreaud and two anonymous reviewers for their very helpful comments.

REFERENCES

Adler, R. F., G. J. Huffman, D. T. Bolvin, S. C. Urtis, and E. J. Nelkin, 2000: Tropical rainfall distributions determined using TRMM combined with other satellite and rain gauge information. *J. Appl. Meteor.,* **39,** 2007–2023.

Baines, P., 1987: Upstream blocking and airflow over mountains. *Annu. Rev. Fluid Mech.,* **19,** 75–97.

Barrett, B. S., R. Garreaud, and M. Falvey, 2009: Effect of the Andes Cordillera on precipitation from a midlatitude cold front. *Mon. Wea. Rev.,* **137,** 3092–3109.

Bousquet, O., and B. F. Smull, 2006: Observed mass transports accompanying upstream orographic blocking during MAP IOP8. *Quart. J. Roy. Meteor. Soc.,* **132,** 2393–2413.

Chiu, L., Z. Liu, H. Rui, and W. Teng, 2006: TRMM data and access tools. *Earth Science Satellite Remote Sensing,* J. Qu et al., Eds., Vol. 2, *Data, Computational Processing, and Tools,* Springer and Tsinghua University Press, 202–219.

Cox, J. A. W., W. J. Steenburgh, D. E. Kingsmill, J. C. Shafer, B. A. Colle, O. Bousquet, B. F. Smull, and H. Cai, 2005: The kinematic structure of a Wasatch Mountain winter storm during IPEX IOP3. *Mon. Wea. Rev.,* **133,** 521–542.

Doyle, J. D., 1997: The influence of mesoscale orography on a coastal jet and rainband. *Mon. Wea. Rev.,* **125,** 1465–1488.

——, and N. A. Bond, 2001: Research aircraft observations and numerical simulations of a warm front approaching Vancouver Island. *Mon. Wea. Rev.,* **129,** 978–998.

Durran, D. R., and J. B. Klemp, 1982: On the effects of moisture on the Brunt–Väisälä frequency. *J. Atmos. Sci.,* **39,** 2152–2158.

Ebuchi, N., H. C. Graber, and M. J. Caruso, 2002: Evaluation of wind vectors observed by QuikSCAT/SeaWinds using ocean buoy data. *J. Atmos. Oceanic Technol.,* **19,** 2049–2062.

Falvey, M., and R. Garreaud, 2007: Wintertime precipitation episodes in central Chile: Associated meteorological conditions and orographic influences. *J. Hydrometeor.,* **8,** 171–193.

Gautier, C., Y. Shiren, and M. D. Hofstader, 2003: AIRS/Vis near IR instrument. *IEEE Trans. Geosci. Remote Sens.,* **41,** 330–342.

Gettelman, A., and Q. Fu, 2008: Observed and simulated upper-tropospheric water vapor feedback. *J. Climate,* **21,** 3282–3289.

——, W. D. Collins, E. J. Fetzer, F. W. Irion, A. Eldering, P. B. Duffy, and G. Bala, 2006: Climatology of upper tropospheric relative humidity from the atmospheric infrared sounder and implications for climate. *J. Climate,* **19,** 6104–6121.

Han, M., S. A. Braun, P. O. G. Persson, and J.-W. Bao, 2009: Alongfront variability of precipitation associated with a mid-latitude frontal zone: TRMM observations and MM5 simulation. *Mon. Wea. Rev.,* **137,** 1008–1028.

Hoskins, B. J., and K. I. Hodges, 2005: A new perspective on Southern Hemisphere storm tracks. *J. Climate,* **18,** 4108–4129.

Hughes, M., A. Hall, and R. G. Fovell, 2009: Blocking in areas of complex topography, and its influence on rainfall distribution. *J. Atmos. Sci.,* **66,** 508–518.

James, C. N., and R. A. Houze, 2005: Modification of precipitation by coastal orography in storms crossing northern California. *Mon. Wea. Rev.,* **133,** 3110–3131.

Jiang, H., and E. J. Zipser, 2010: Contribution of tropical cyclones to the global precipitation from eight seasons of TRMM data: Regional, seasonal, and interannual variations. *J. Climate,* **23,** 1526–1543.

Kalnay, E., and Coauthors, 1996: The NCEP/NCAR 40-Year Reanalysis Project. *Bull. Amer. Meteor. Soc.,* **77,** 437–470.

Kummerow, C., W. Barnes, T. Kozu, J. Shiue, and J. Simpson, 1998: The Tropical Rainfall Measuring Mission (TRMM) sensor package. *J. Atmos. Oceanic Technol.,* **15,** 809–817.

Kurz, M., 1990: The influence of the Alps on structure and behaviour of cold fronts over southern Germany. *Meteor. Atmos. Phys.,* **43,** 61–68.

Labraga, J. C., O. Frumento, and M. López, 2000: The atmospheric water vapor cycle in South America and the tropospheric circulation. *J. Climate,* **13,** 1899–1915.

Lackmann, G. M., and J. E. Overland, 1989: Atmospheric structure and momentum balance during a gap-wind event in the Shelikof Strait, Alaska. *Mon. Wea. Rev.,* **117,** 1817–1833.

Marwitz, J. D., 1987: Deep orographic storms over the Sierra Nevada. Part I: Thermodynamic and kinematic structure. *J. Atmos. Sci.,* **44,** 159–173.

Mass, C. F., and G. K. Ferber, 1990: Surface pressure perturbations produced by an isolated mesoscale topographic barrier. Part I: General characteristics and dynamics. *Mon. Wea. Rev.,* **118,** 2579–2596.

Miller, A., 1976: The climate of Chile. *World Survey of Climatology,* W. Schwerdtfeger, Ed., Vol. 12, *Climates of Central and South America,* Elsevier Scientific Publishing, 113–130.

O'Handley, C., and L. F. Bosart, 1996: The impact of the Appalachian Mountains on cyclonic weather systems. Part I: A climatology. *Mon. Wea. Rev.,* **124,** 1353–1373.

Overland, J. E., 1984: Scale analysis of marine winds in straits and along mountainous coasts. *Mon. Wea. Rev.,* **112,** 2532–2536.

Parish, T. R., 1982: Barrier winds along the Sierra Nevada Mountains. *J. Appl. Meteor.,* **21,** 925–930.

Raja, M. K. R. V., S. I. Gutman, J. G. Yoe, L. M. McMillin, and J. Zhao, 2008: The validation of AIRS retrievals of integrated precipitable water vapor using measurements from a network of ground-based GPS receivers over the contiguous United States. *J. Atmos. Oceanic Technol.,* **25,** 416–428.

Rozante, J. R., D. S. Moreira, L. G. G. de Goncalves, and D. A. Vila, 2010: Combining TRMM and surface observations of precipitation: Technique and validation over South America. *Wea. Forecasting,* **25,** 885–894.

Ryoo, J., D. W. Waugh, and A. Gettelman, 2008: Variability of subtropical upper tropospheric humidity. *Atmos. Chem. Phys. Discuss.,* **8,** 1041–1067.

Smith, R. B., 1979: The influence of mountains on the atmosphere. *Advances in Geophysics,* Vol. 21, Academic Press, 183–186.

Viale, M., and F. A. Norte, 2009: Strong cross-barrier flow under stable conditions producing intense winter orographic precipitation: A case study over the subtropical central Andes. *Wea. Forecasting,* **24,** 1009–1031.

Xavier, P. K., V. O. John, S. A. Buehler, R. S. Ajayamohan, and S. Sijikumar, 2010: Variability of Indian summer monsoon in a new upper tropospheric humidity data set. *Geophys. Res. Lett.,* **37,** L05705, doi:10.1029/2009GL041861.

Yu, C.-K., and B. F. Smull, 2000: Airborne observations of a land-falling cold front upstream of steep coastal orography. *Mon. Wea. Rev.,* **128,** 1577–1603.

——, and N. A. Bond, 2002: Airborne Doppler observations of a cold front in the vicinity of Vancouver Island. *Mon. Wea. Rev.,* **130,** 2692–2708.